IEEE Access
Multidisciplinary | Rapid Review | Open Access Journal

Received April 2, 2021, accepted April 17, 2021, date of publication April 26, 2021, date of current version May 4, 2021.

Digital Object Identifier 10.1109/ACCESS.2021.3075495

Design and Analysis of Dual Polarized Broadband Microstrip Patch Antenna for 5G mmWave Antenna Module on FR4 Substrate

GYOUNGDEUK KIM AND SANGKIL KIM, (Senior Member, IEEE)
Department of Electrical and Electronic Engineering, Pusan National University, Busan 46241, South Korea

Corresponding author: Sangkil Kim (ksangkil3@pusan.ac.kr)

This work was supported in part by the National Research Foundation of Korea (NRF) grant funded by the Korea Government (MSIT) under Grant 2020R1C1C1003362, and in part by Samsung Electronics Company Ltd.

ABSTRACT This study presents a dual polarized broadband microstrip patch antenna for a 5G mmWave antenna module on an FR4 substrate. The proposed antenna was fabricated using a standard FR4 printed circuit board (PCB) process because of its low cost and ease of mass production. The electrical properties of the FR4 substrate in the 5G mmWave frequency band were also characterized. An air cavity structure was introduced to mitigate the high loss tangent of the FR4 substrate. Capacitive elements such as proximity L-probe feedings and parasitic patches are used to improve the impedance bandwidth of the patch antenna. For the polarization diversity of the massive multiple-input multiple-output (MIMO) capability, the antenna radiator was designed with a symmetrical structure, and the relative position of the L-probes excites the orthogonal resonant modes to enable dual linear polarization. The operation principle of the proposed antenna was thoroughly analyzed by characteristic mode analysis (CMA). The measured bandwidth of a single antenna was 23.1 % (23 $\sim$ 29 GHz) and the gain value was 5 dBi. The measured cross-polarization suppression ratio of single antenna was 15 $\sim$ 20 dB. The measured gain value of 1 $\times$ 4 antenna array was 10 $\sim$ 11 dBi and the cross-polarization suppression ratio was about 20 dB. The size of the proposed single antenna is $0.41\lambda_0 \times 0.41\lambda_0 \times 0.1\lambda_0$, and that of a 1 $\times$ 4 antenna array is $2.78\lambda_0 \times 0.41\lambda_0 \times 0.1\lambda_0$. The envelope correlation coefficient (ECC) was calculated and was lower than 0.02 in the 5G mmWave frequency band.

INDEX TERMS 5G mmWave antenna, massive MIMO, FR4 PCB, array antenna, characteristic mode analysis, broadband patch antenna, dual polarized patch antenna.

I. INTRODUCTION

With the proliferation of mobile devices like smartphones, mobile data traffic has increased significantly. One of the key elements consisting of the 4th industrial revolution (or Industry 4.0), such as smart hospitals, smart factories, and autonomous vehicles, is next-generation communication standards (*i.e.*, 5G, Beyond 5G, and 6G), which require extremely low latency and a high data rate. Recently, 5G mmWave technology has been attracting great attention from numerous researchers and industries because of its extremely high data rate of up to several Gbps and ultra-low latency of several *ms* [1]–[5]. A key element in realizing mmWave technology is a high-performance RF front-end (RFFE) system for mobile devices or base stations. However, meeting all the design specifications for RFFE systems in mobile devices is a challenging task because of their small form factor and limited available RF power. The system-in-package (SiP) technology is an essential technology for cutting-edge RFFE modules due to its advantages of signal/power loss reduction and high system integrity [6]–[9]. Multiple functional integrated circuits (ICs) and passive components, such as power-management integrated circuits (PMICs), radio frequency integrated circuits (RFIC), and SMDs, are integrated on a single package substrate (or laminate). It results in dramatic loss reduction due to the short physical distance between the components. EM fields in the mmWave frequency band can be also tightly confined within the RFFE module. For a 5G mmWave RFFE mobile module applications, antennas are usually implemented in the package (antenna-in-package, AiP) because the half-wave length ($\lambda_0/2$) in the 5G mmWave frequency band is comparable to

The associate editor coordinating the review of this manuscript and approving it for publication was Shah Nawaz Burokur.

the size of RFFE modules [10]. The antenna of the RFFE module is a critical component that should be designed carefully to have high performance as well as meet challenging system requirements (*e.g.* bandwidth, form factor, gain, radiation patterns, etc.).

Many novel 5G mmWave antenna designs have been reported [11]–[15]. The antenna bandwidth and gain were improved by using a high-K dielectric superstrate [11], [12]. A broadband low-profile antenna was proposed using a vertically folded slotted circular patch antenna [13]. The operation bandwidth was improved by introducing a coupled feeding structure. A corporate stacked BW_{3dB} microstrip antenna was fed by slot-coupled substrate integrated waveguide (SIW) feeding networks [14]. Antenna gain and bandwidth were improved by applying a stacked patch topology and a substrate integrated cavity composed of via walls [15]. Most of the reported research efforts have used high-cost Teflon or ceramic based low-loss materials. These low-loss materials are usually expensive and make up a significant portion of the price of mmWave modules.

The main novelty of this paper is the systematic design of a high-performance low-cost antenna for 5G mmWave AiP module based on characteristic mode analysis (CMA) method. In this paper, a dual polarized broadband microstrip patch antenna for 5G mmWave applications on low-cost FR4 substrate is presented to implement a high-performance mmWave antenna on low-cost high-loss material. The proposed antenna was fabricated by a FR4 PCB process since it is a well-developed cost-effective process. Low-loss and low-cost alternative materials, such as F4BM, are good choices for reducing cost and signal loss, but in this study, high-loss FR4 material is chosen to demonstrate a systematic design approach for dielectric loss mitigation and broadband patch antenna design. The proposed antenna design covers most international commercial 5G mmWave frequency bands and features polarization diversity (dual polarization) for massive multiple-input multiple-output (MIMO) capability [16]. The operation principle of the proposed antenna was analyzed by CMA.

This paper is organized as follows. In Section II, the electrical properties of the FR4 substrate are characterized by the T-resonator method since an accurate electrical model of the substrate is essential to design a high-performance antenna. In Section III, the design and analysis of the proposed single/array antenna are presented. Detailed antenna geometry, thorough theoretical analysis, and CMA are discussed. The measured performance parameters of the proposed antenna in the 5G mmWave band, such as the antenna gain, $|S_{11}|$, and Envelope Correlation Coefficient (ECC), are compared to simulation results in Section IV. This is followed by the conclusion.

II. FR4 CHARACTERIZATION

Accurate electrical properties of the FR4 substrate in the mmWave frequency band are critical information for designing high-performance antennas. However, the electrical properties of FR4 substrate have not been reported for the 5G mmWave frequency band (24 $\sim$ 29 GHz). Thus, the T-resonator method was adopted to extract the relative dielectric constant (ε_r) and loss tangent (tan δ) of the FR4 substrate. The T-resonator consists of a simple T-pattern with a microstrip open stub and feeding lines. The length (L) of the open stub can be determined by the quarter-wave ($\lambda_g/4$) resonator design equation:

$$L = \frac{n \cdot c}{4f\sqrt{\varepsilon}_{eff}} \tag{1}$$

where n is the order of the resonance ($n = 1, 3, 5,...$), c is the speed of light, f is the resonance frequency, and effective dielectric constant (ε_{eff}) is the effective dielectric constant [17]. Fig. 1 shows the fabricated T-resonator on 200-μm-thick FR4 substrate (H). The width (W) and thickness of the metal are 0.4 mm and 16 μm, respectively.

The T-resonator method extracts ε_r and tan δ of materials from odd harmonic resonance modes of the T-shaped microstrip $\lambda_0/4$ open stub resonator as shown in Fig. 1. In general, the T-resonator should be designed to resonate at a frequency point lower than the desired frequency band to get as much data as possible. In this work, for instance, a fundamental mode of the T-resonator was designed to resonate at 1 GHz ($L = 45\ mm$). The designed T-resonator resonated at each odd harmonic (1 GHz, 3 GHz, 5GHz, $\sim$ etc.) to obtain ε_r and tan δ with a 2 GHz step. Table 1 shows the measured resonance frequency points of the designed T-resonator and the 3-dB bandwidth.

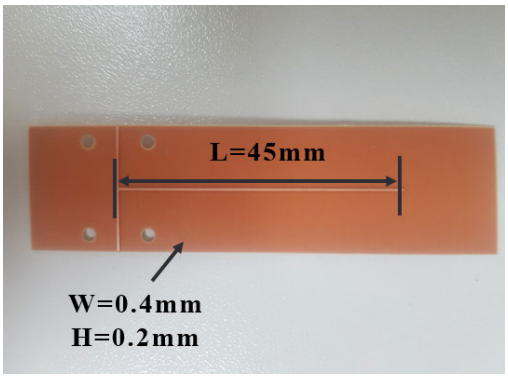

FIGURE 1. Fabricated microstrip T-resonator on FR4 substrate.

TABLE 1. T-resonator measurement.

Resonance Frequency (GHz)	BW_{3dB} (GHz)
23.27	0.75
25.04	0.82
26.81	0.99
28.67	1.36
30.70	1.21
32.41	1.04

The effective dielectric constant can be calculated using the resonance frequency points and the electrical length of the stub. The effective dielectric constant was extracted using the measured values in Table 1 and equation (2)

$$\varepsilon_{eff}(n) = \left[\frac{n \cdot c}{4\left(L + \frac{W}{2} + l_{eo} - d_2\right) f(n)}\right]^2 \tag{2}$$

where L and W are the length of the stub and the physical width of the feed line, respectively. The correction factors for the effects of the open end and T-junction are l_{eo} and d_2, respectively [17].

$$l_{eo} = \frac{abk}{d}h \tag{3}$$

where

$$a = 0.43\left[\frac{\varepsilon_{eff}^{0.81} + 0.26}{\varepsilon_{eff}^{0.81} - 0.19}\right]\left[\frac{(W/H)^{0.85} + 0.24}{(W/H)^{0.85} + 0.87}\right] \tag{4}$$

$$g = 1 + \frac{(W/H)^{0.37}}{2.4\varepsilon_r + 1} \tag{5}$$

$$b = 1 + 0.53\frac{\tan^{-1}\left(0.084\,(W/H)^{1.94/g}\right)}{\varepsilon_{eff}^{0.92}} \tag{6}$$

$$k = 1 - 0.22e^{-7.5W/H} \tag{7}$$

$$d = 1 + 0.038\tan^{-1}\left(0.067(W/H)^{1.48}\right) \times \left(6 - 5e^{0.036(1-\varepsilon_r)}\right) \tag{8}$$

$$\frac{d_2}{W_{eff}} = 0.5 - \left(0.05 + 0.7e^{-1.6} + 0.25\left(f/f_{p1}\right)^2\right) \tag{9}$$

where W_{eff} is the effective width of W, and f_{p1} is the frequency of the first-order (dominant) resonance mode. The ε_r of a transmission line is calculated using (10).

$$\varepsilon_{eff} = \frac{\varepsilon_r + 1}{2} + \frac{\varepsilon_r - 1}{2}\left[\frac{1}{\sqrt{1 + 12\,(H/W)}} + 0.04\,(1 - W/H)^2\right] \quad \frac{W}{H} < 1$$

$$\varepsilon_{eff} = \frac{\varepsilon_r + 1}{2} + \frac{\varepsilon_r - 1}{2\sqrt{1 + 12\left(\frac{H}{W}\right)}} \quad \frac{W}{H} > 1 \tag{10}$$

The calculated relative dielectric constant of the FR4 substrate is shown in Fig. 2. The relative dielectric constant (ε_r) increases as the frequency increases in the frequency band of interest (24 $\sim$ 29 GHz).

The tan δ is extracted from the unloaded quality factors (Q-factor) of the T-resonator. The unloaded quality factor (Q_0) is calculated as follows:

$$Q_L = \frac{f}{BW_{3dB}} \tag{11}$$

$$Q_0 = \frac{Q_L}{\sqrt{1 - 2 \cdot 10^{-(L_A/10)}}} \tag{12}$$

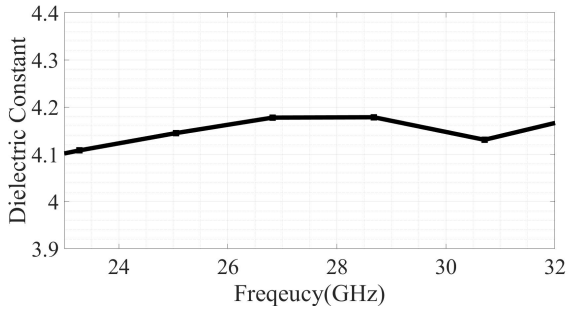

FIGURE 2. Extracted relative dielectric constant (εr) of FR4 substrate.

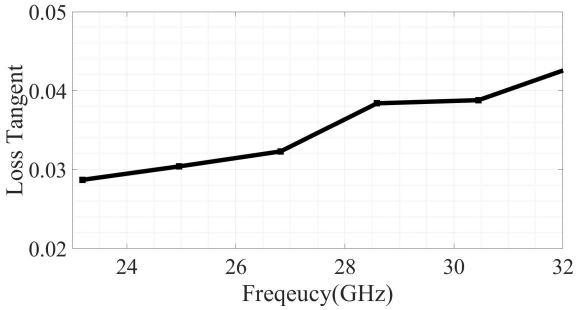

FIGURE 3. Extracted loss tangent (tan δ) of FR4 substrate.

where Q_L is the loaded quality factor and L_A is the value of insertion loss (IL) at the resonant frequency. f and BW_{3dB} are the measured resonance frequency and the 3-dB bandwidth, respectively. The unloaded quality factor consists of dielectric material (Q_d), conductor (Q_c) and radiation losses (Q_r). Q_d can be calculated by (13) [17].

$$\frac{1}{Q_0} = \frac{1}{Q_d} + \frac{1}{Q_c} + \frac{1}{Q_r} \tag{13}$$

The tan δ is calculated by Q-factors of the dielectric material and the previously calculated dielectric constant, as shown in (14).

$$\tan\delta = \frac{\varepsilon_{eff}(\varepsilon_r - 1)}{Q_d\varepsilon_r(\varepsilon_{eff} - 1)} \tag{14}$$

The measured tan δ of the substrate in the 5G mmWave frequency band is shown in Fig. 3. Like the relative dielectric constant, the tan δ values also tend to increase with increasing frequency.

III. ANTENNA DESIGN AND ANALYSIS

A. 5G mmWave ANTENNA MODULE FOR MOBILE DEVICES

Antenna performance is a key design parameter of an AIP module for mobile devices, and it is critical to design a high-performance antenna satisfying all the design requirements. Table 2 summarizes the target antenna performance specifications presented in this paper. The antenna array gain should be higher than 10 dBi to maintain a robust communication link because of the high free space path loss [1]-[3]. The target

TABLE 2. Proposed antenna specifications.

Specification	Design Target
Array Antenna Gain	> 10 dBi
Freq. Bandwidth ($\|S_{11}\|$ < -10 dB)	24 ~ 29 GHz
ECC	< 0.3
Radiation Pattern	Broadside radiation
Polarization	Dual (H&V)

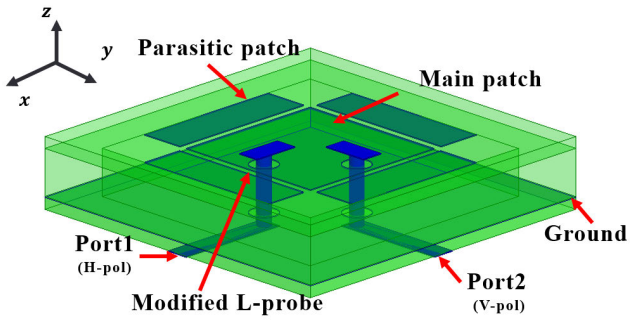

FIGURE 4. Geometry of the proposed dual polarized broadband patch antenna.

fractional impedance bandwidth should be broader than 19 % at 26.5 GHz (24 ~ 29 GHz) to cover multiple international 5G mmWave frequency bands, including those of China (24.75 ~ 27.5 GHz), Europe (24.5 ~ 27.5 GHz), and South Korea (26.5 ~ 28.9 GHz).

The antennas for a 5G mmWave module should be able to support massive MIMO functionality to improve the spectral efficiency of 5G and Beyond 5G communication. The antennas should have dual polarization (V-/H-polarizations) properties, and the isolation level between the V-pol and H-pol is critical. The isolation level can be characterized by the ECC rather than simple S-parameters between ports. For massive MIMO, ECC should be less than 0.5, but the design target of ECC is set to 0.3 or less in consideration of the design margin [18]. The proposed antenna was fabricated by a conventional FR4 PCB manufacturing process because it is cost-effective and well-developed.

There are two main issues in designing a planar patch antenna on FR4 substrate while satisfying all the design requirements: i) the high loss tangent value of FR4 substrate and ii) the narrow bandwidth of a planar patch antenna. An air cavity structure under the main patch radiator shown in Fig. 4 and 5 minimizes dielectric loss and increases bandwidth [19],[20]. This is done because the excited EM fields of the antenna are concentrated in the air cavity. The radiation efficiency of the antenna can also be significantly improved since the interaction of the EM field and the lossy FR4 substrate is minimized. For the broadband properties, capacitive elements, such as parasitic patches and proximity L-probe feeding structures are used in the patch antenna, as shown in Fig. 5 [21].

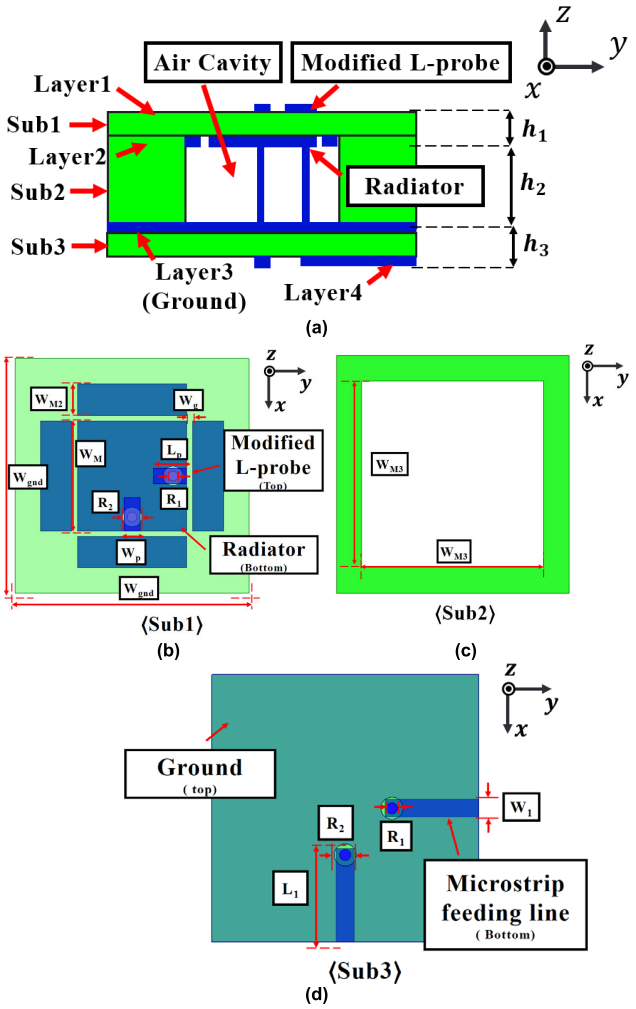

FIGURE 5. Configuration of the proposed antenna: (a) side view of antenna, (b) top view of sub1(layer1-top, layer2-bottom), (c) top view of sub2 and (d) top view of sub3(layer3-top, Layer4-bottom).

B. ANTENNA GEOMETRY

Fig. 4 shows the geometry of the proposed antenna. Four parasitic patches were used in the main radiator, and the L-probe was placed on top of the antenna for ease of fabrication [22]. Fig. 5 shows a side view and the detailed structure of the antenna. The values of the design parameters are listed in Table 3. All the layers shown in Fig. 5 were fabricated by a conventional low-cost FR4 PCB process. The antenna consists of three substrates, with heights of $h_1 = 0.2$ mm, $h_2 = 0.8$ mm, and $h_3 = 0.2$ mm. 16 μm-thick copper foil was printed on the FR4 substrate. Fig. 5(b) shows the location of the L-probe placed on top of Sub1 and the radiation patch is placed on the bottom side to simplify the fabrication process. Fig. 5(c) shows a dielectric spacer (Sub2) for air cavity structure. Ground plane and antenna feeding networks were printed on the top and bottom of Sub3 as shown in Fig. 5(d). The width (W_1) of the feed line was designed to be 50 Ω. A vertical cylindrical wire with a diameter (R_1) of 0.25 mm connects the L-probe to the feeding networks on L3.

TABLE 3. Antenna design parameters.

Parameter	W_M	W_c	W_{M3}	W_g	W_a	W_l
Value (*mm*)	2.8	0.8	4.7	0.15	6.0	0.4
Parameter	L_1	W_P	L_P	R_1	R_2	W_{gnd}
Value (*mm*)	2.2	0.4	0.85	0.25	0.5	6
Parameter	h_1	h_2	h_3			
Value (*mm*)	0.2	0.8	0.2			

C. CHARACTERISTIC MODE ANALYSIS (CMA)

The operation principle of the proposed antenna can be explained by the CMA [23]–[26]. CMA provides insights into the physical characteristics of an antenna structure. The basis currents from CMA are orthogonal to each other, resulting in orthogonal far-field radiation patterns. The basis currents are called characteristic currents ($\boldsymbol{J}_n$), and the total current ($\boldsymbol{J}$) on a conducting body is the sum of all the characteristic currents:

$$\boldsymbol{J} = \sum_{n=1}^{\infty} \alpha_n \boldsymbol{J}_n \tag{15}$$

where α_n is the modal weighting coefficient (MWC) of the n-th characteristic mode current. $\boldsymbol{J}_n$ is calculated by the following generalized eigenvalue problem:

$$[\mathrm{X}]\,[\boldsymbol{J}_n] = \lambda_n\,[\mathbf{R}]\,[\boldsymbol{J}_n] \tag{16}$$

where $[\mathbf{X}]$ and $[\mathbf{R}]$ are the imaginary and real parts of the method of moments (MoM) impedance matrix ($[\mathbf{Z}]=[\mathbf{R}]+[\mathbf{X}]$).

Resonance occurs when an eigenvalue (λ_n) is zero. At this point, the radiated energy is the maximum value, while the stored energy is the minimum [27]. The n-th MWC can be determined by equation (17) with λ_n of the n-th characteristic eigenvalue equation:

$$\alpha_n = \frac{\langle \boldsymbol{J}_n, \boldsymbol{E}^i_{tan} \rangle}{1 + j\lambda_n} \tag{17}$$

where $\boldsymbol{E}^i_{tan}$ is the incident tangential E-field on the conducting body, and the $\langle\cdot\rangle$ operator indicates the inner product. All eigenvalues (λ_n) and characteristic currents ($\boldsymbol{J}_\mathrm{n}$) are real numbers because $[\mathbf{R}]$ and $[\mathbf{X}]$ are real and symmetric matrices. The modal significance (MS) and modal excitation coefficient (MEC) are the denominator and numerator of (17) as shown in (18) and (19).

$$\mathrm{MS} = \left| \frac{1}{1 + j\lambda_n} \right| \tag{18}$$

$$\mathrm{MEC} = \langle \boldsymbol{J}_n, \boldsymbol{E}^i \rangle \tag{19}$$

Thus, all the characteristic currents (or characteristic modes) satisfy the following orthogonal properties shown in (20) $\sim$ (22)

$$\langle \boldsymbol{J}_m, R\boldsymbol{J}_n \rangle = \delta_{mn} \tag{20}$$

$$\langle \boldsymbol{J}_m, X\boldsymbol{J}_n \rangle = \lambda_n \delta_{mn} \tag{21}$$

$$\langle \boldsymbol{J}_m, Z\boldsymbol{J}_n \rangle = (1 + j\lambda_n)\,\delta_{mn} \tag{22}$$

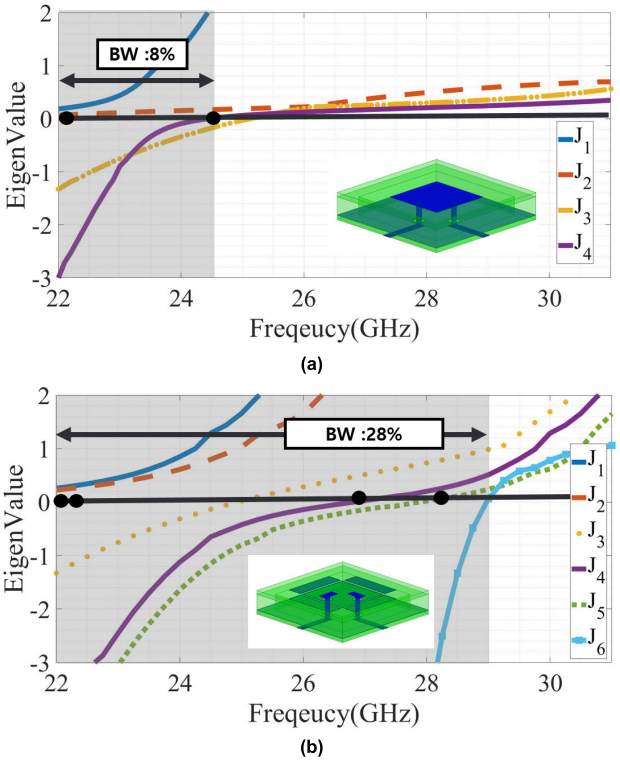

FIGURE 6. Eigenvalue (λ_n) of antennas: (a) square patch antenna and (b) square patch antenna with proximity L-probe feedings and parasitic patches.

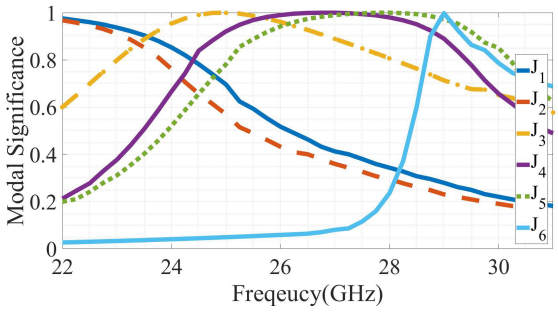

FIGURE 7. Modal significance (MS) of the proposed antenna.

where R, X, and Z are elements of the $[\mathbf{R}]$, $[\mathbf{X}]$, and $[\mathbf{Z}]$ matrices, respectively. δ_mn is the Kronecker delta function.

A new set of eigenvalues, μ_n, is introduced when reactive elements ($[\mathbf{X}_\mathrm{L}]$) are loaded in the conducting body, as shown in (23) and (24):

$$[\mathbf{X} + \mathbf{X}_L]\,[\boldsymbol{J}_n] = \mu_n\,[\mathbf{R}]\,[\boldsymbol{J}_n] \tag{23}$$

$$\mu_n = \lambda_n + [\boldsymbol{X}_L]\,[\mathbf{R}]^{-1} \tag{24}$$

The new eigenvalue, μ_n, can be controlled by the types of reactive loadings as shown in (25)

$$X_L = \begin{cases} 2\pi f L & (X_L > 0) \\ -\dfrac{1}{2\pi f C} & (X_L < 0) \end{cases} \tag{25}$$

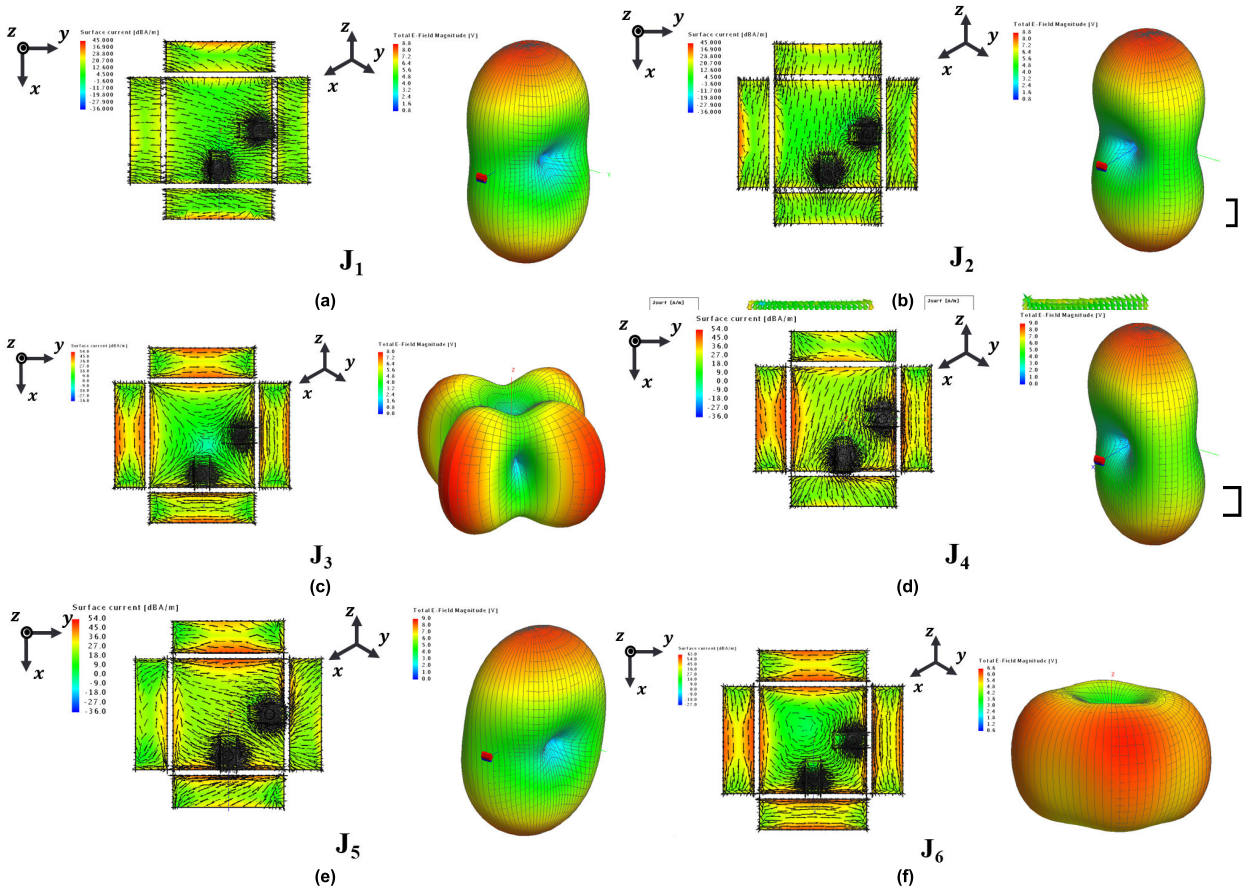

FIGURE 8. CM current distribution and E-field pattern of each characteristic mode: (a) J_1 at 22 GHz, (b)J_2 at 22 GHz, (c) J_3 at 25 GHz, (d)J_4 at 27 GHz, (e)J_5 at 28 GHz and (f)J_6 at 29GHz.

where X_L is the elements of matrix $[\mathbf{X}_L]$. From (24) and (25), the resonant frequency of the characteristic current can be shifted to a lower or higher frequency by controlling the reactive loadings [27], [28].

Resonant frequencies of higher-order characteristic mode were shifted to lower desired resonant frequencies by capacitive loadings, such as the proximity L-probe feeding and parasitic patches, to increase the impedance bandwidth of the planar patch antenna. As a proof of concept and without loss of generality, CMA was used to analyze the characteristic modes of a simple coax-fed patch antenna and the proposed proximity L-probe fed patch antenna with parasitic patches, as shown in Fig. 6. The characteristic modes were calculated using Altair FEKO. Only four resonating characteristic modes (CMs) were observed at the frequency band of interest for the simple square patch antenna as shown in Fig. 6(a). However, two more CMs were newly introduced, and the CMs interval was modified to expand the bandwidth of the proposed antenna as shown in Fig. 6(b). Fig. 7 shows the MS of the proposed patch antenna with capacitive loadings (L-probe and parasitic patches). It shows that CM currents, $\boldsymbol{J}_1 \sim \boldsymbol{J}_6$, contribute to the radiation of the proposed antenna.

Fig. 8 shows modal surface current distribution and E-field pattern due to the CM currents of the proposed patch antenna structure. The CMs resonating in the parasitic patch are $\boldsymbol{J}_1$, $\boldsymbol{J}_2$, and the CMs generated due to the coupling of the main patch and the parasitic patch are $\boldsymbol{J}_4$, $\boldsymbol{J}_5$. It is clear that $\boldsymbol{J}_1$ and $\boldsymbol{J}_2$ are CM currents of TM_{10} modes in x- and y- directions, respectively. $\boldsymbol{J}_4$ and $\boldsymbol{J}_5$ are CM currents of Quasi-TM_{30} mode. The loading effect of the parasitic patches is also observed because the strong CM currents flow on the parasitic patches. $\boldsymbol{J}_3$ is the CM current of the ground plane ($W_{gnd} \times W_{gnd}$) which do not contribute to the antenna radiation. $\boldsymbol{J}_6$ resonates in all patches, so it has a broadside radiation pattern. $\boldsymbol{J}_1$, $\boldsymbol{J}_5$ resonate the Y-pol of the proposed antenna, and $\boldsymbol{J}_2$, $\boldsymbol{J}_4$ resonate the X-pol. In this work, the L-probes are designed to excite only $\boldsymbol{J}_1$, $\boldsymbol{J}_2$, $\boldsymbol{J}_4$, and $\boldsymbol{J}_5$ which has the desired radiation patterns over the broad frequency band. The L-probes in x- or y-axis excites corresponding x- or y-polarized waves. Fig. 9 shows the sum of CM currents excited by the vertical probe (x-axis direction). CM currents at each frequency are

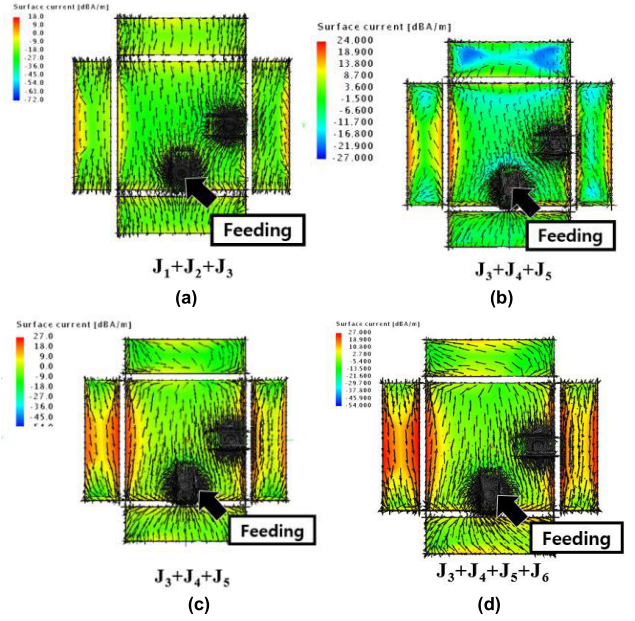

FIGURE 9. Sum of CM currents excited by the vertical probe: (a) 22 GHz, (b) 25 GHz, (c) 27 GHz and (d) 29 GHz.

chosen according to the magnitude of the MS values shown in Fig. 7. For instance, MS values of $\boldsymbol{J_3}$, $\boldsymbol{J_4}$, and $\boldsymbol{J_5}$ at 27 GHz are much higher than other CM currents, and those values are summed up. It is found that the x-axis probe excites $\boldsymbol{J}_2$ and $\boldsymbol{J}_4$ dominantly.

The proposed antenna was also investigated using the total surface current distribution ($\boldsymbol{J}$) as shown in Fig. 10. The surface current distributions were computed by Ansys HFSS release 19. The total current distributions shown in Fig. 10 correspond to the sum of excited characteristic current modes shown in Fig. 9. At 22 GHz, most of the total surface current flows on the edges of parasitic patches since it is resonating in TM_{10} mode as shown in Fig. 10(a). At 25, 27 and 29 GHz, most of the total surface currents flow on the main and parasitic patches to form a quasi-TM_{30} mode [29]. Field distributions of TM_{10} and quasi-TM_{30} modes under the radiation patches are depicted in Fig. 10(e) and (f).

D. 1 × 4 ANTENNA ARRAY

A 1×4 dual polarized antenna array is designed with the configuration shown in Fig. 11. Like the proposed single antenna element, the antenna array consists of three substrates with the same thickness. The distance (L) between the antenna array elements is set to 9.5 *mm* based on linear antenna array theory [30]. The drill holes in each substrate are perforated for alignment. A feeding network for the antenna array is printed on the bottom of Sub3. Fig. 12(b) shows the half plane of the antenna array feeding network for measurement. It matches from 50 Ω to 100 Ω through a linear tapered microstrip line $L_t = 4.8\ mm\ (\cong 3/4\lambda_g)$.

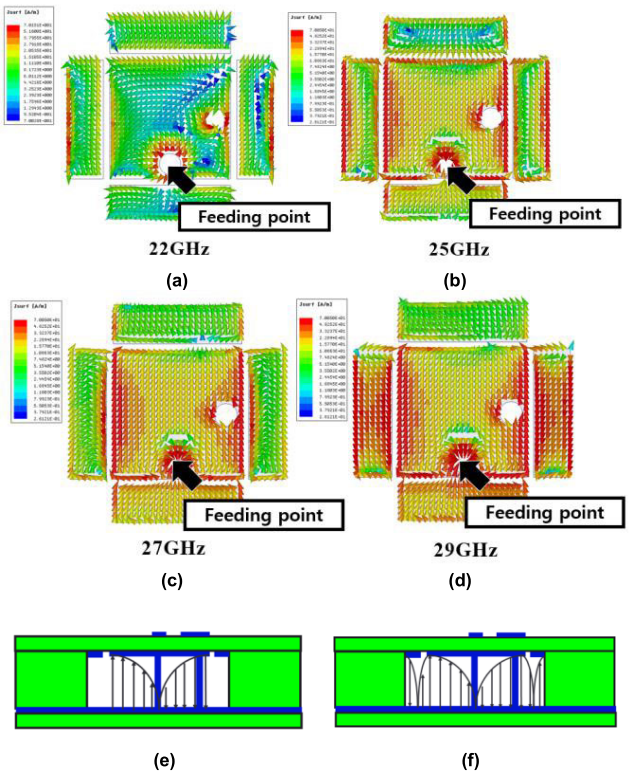

FIGURE 10. Total surface current distributions at (a) 22 GHz (TM_{10}), (b) 25 GHz (quasi-TM_{30}), (c) 27 GHz (quasi-TM_{30}), (d) 29 GHz (quasi-TM_{30}), and field distributions of (e) TM_{10} and (f) quasi-TM_{30} modes.

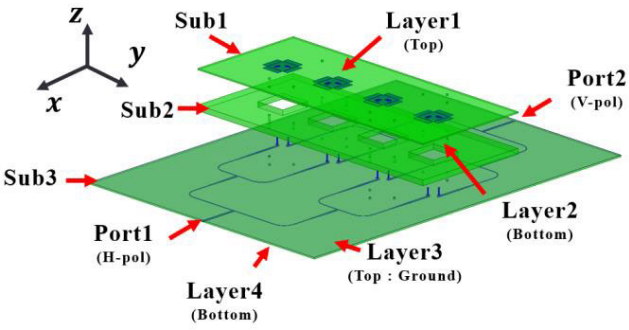

FIGURE 11. 3D geometry of the proposed dual polarized 1 × 4 antenna array.

IV. ANTENNA MEASUREMENT

The proposed antenna was fabricated using the FR4 PCB process shown in Fig. 13. All the layers were assembled using nylon bolts and nuts for ease of fabrication. The red boxes in Fig. 13 indicate antennas, and the rest are feeding networks and connectors for measurements. All the antennas were measured in an anechoic chamber.

A. SINGLE ANTENNA ELEMENT

The measured and simulated reflection coefficients ($|S_{11}|$, $|S_{22}|$) are shown in Fig. 14. The −10dB impedance bandwidth

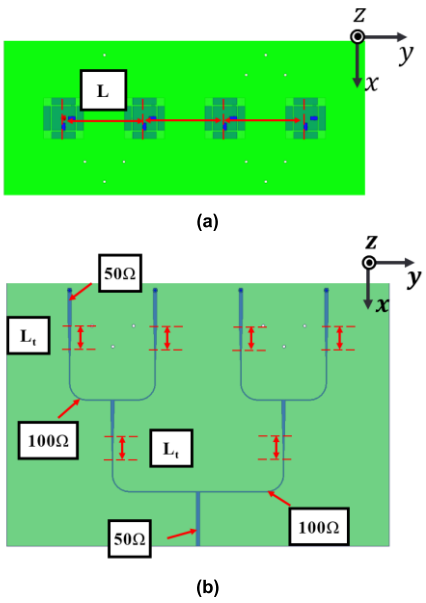

FIGURE 12. Configuration of the proposed 1 × 4 array antenna: (a) Top view of sub1(layer1-top, layer2-bottom) and (b) 1 × 4 feeding network.

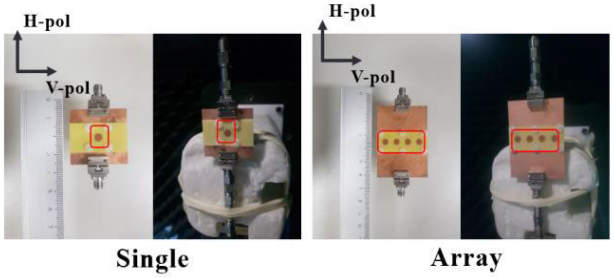

FIGURE 13. Fabricated antennas and measurement environment.

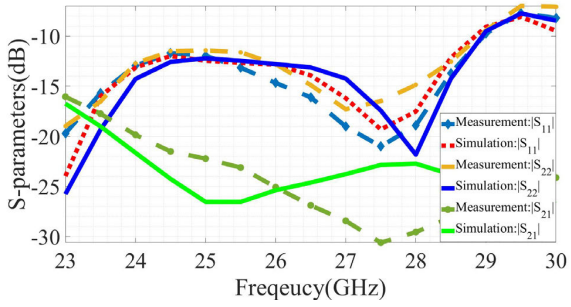

FIGURE 14. Measured S-parameter of the proposed single antenna.

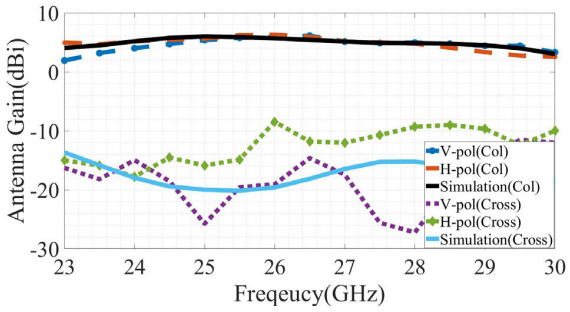

FIGURE 15. Measured gain of the proposed single antenna element.

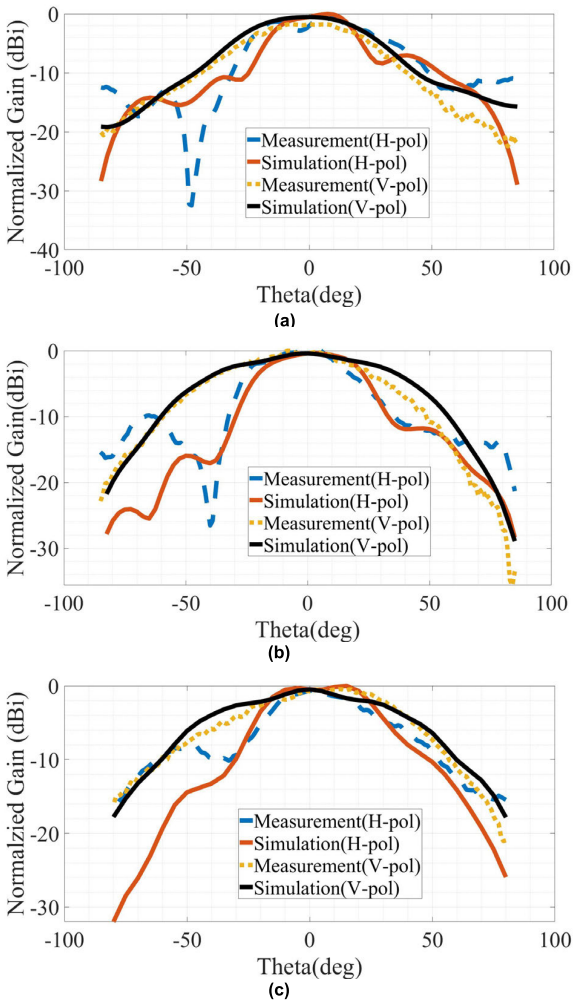

FIGURE 16. Measured radiation patterns of the proposed single antenna element at (a) 24 GHz, (b) 26 GHz, and (c) 28 GHz.

is about 23.1 % (23 ∼ 29 GHz) and covers the design target of the 5G mmWave band at 24 ∼ 29 GHz. The measured and simulation values match well. The discrepancy between the measurement and simulation is due to the fabrication error of the radius R_1 shown in Fig. 5. Critical errors were observed when the vertical wire connecting the feedline and the L-probe was tilted.

Fig. 15 shows the measured and simulated antenna gain values with respect to the frequency. The measured cross polarization suppression was about 15 ∼ 20 dB in the frequency band of interest. Fig. 16 shows the measured radiation patterns at 24, 26, and 28 GHz, and they match very well. The small discrepancy at the H-pol pattern is due to the × connector and feeding coaxial lines for the measurement. The ECC value which represents isolation between the vertical and horizontal polarizations for polarization diversity of massive MIMO is 0.017 ∼ 0.0003 in 23 ∼ 30 GHz band. The proposed antenna's ECC is much lower than the required value. The measured radiation efficiency of the

TABLE 4. 5G mmWave antenna performance comparison.

	[11]	[13]	[14]	[15]	Proposed Antenna
Type	Patch	Patch	Patch	Patch	Patch
Array Size	1×4	2×2	2×2	1×8	1×4
Array Antenna Gain	16 dBi	13.7 dBi	11.7 dBi	16.7 dBi	11 dBi
Substrate Material	RT5880 ($tan\delta = 0.0009$ $\varepsilon_r = 2.2$)	RO4450B ($tan\ \delta = 0.004$ $\varepsilon_r = 3.54$) TLY-5 ($tan\delta = 0.0009$ $\varepsilon_r = 2.2$)	TLY-5 ($tan\ \delta = 0.0009$ $\varepsilon_r = 2.2$) RO4450B ($tan\delta = 0.004$ $\varepsilon_r = 3.54$)	Prepreg: ISOLA IS300MD ($tan\ \delta = 0.0033$ $\varepsilon_r = 3.67$) Core: EMC EM355(D) ($tan\ \delta = 0.011$ $\varepsilon_r = 3.3$)	FR4 ($tan\ \delta = 0.03$ $\varepsilon_r = 4.1{\sim}4.2$)
Bandwidth	27 ~ 32 GHz	26.4 ~ 32.3 GHz	25.4 ~ 30.8 GHz	25.75 ~ 30.1 GHz	23 ~ 29 GHz
Antenna Size	$4.16\lambda_0{\times}0.56\lambda_0{\times}0.54\lambda_0$	$1.48\lambda_0{\times}1.48\lambda_0{\times}0.083\lambda_0$	$1.85\lambda_0{\times}1.85\lambda_0{\times}0.083\lambda_0$	$5.65\lambda_0{\times}0.75\lambda_0{\times}0.093\lambda_0$	$2.78\lambda_0{\times}0.41\lambda_0{\times}0.1\lambda_0$
Polarization	Single	Single	Single	Dual	Dual

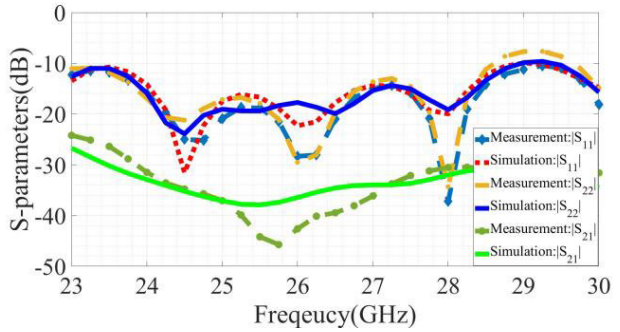

FIGURE 17. Measured S-parameters of the proposed 1 × 4 antenna array.

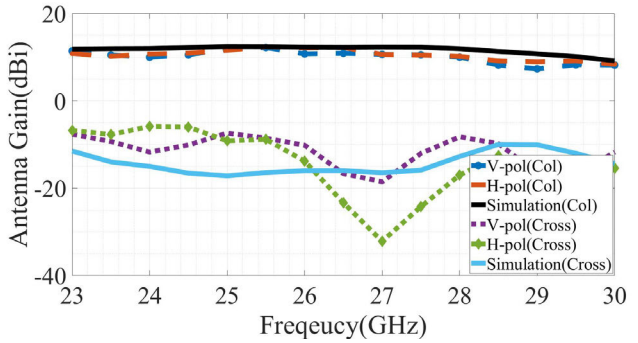

FIGURE 18. Measured antenna gain of the proposed 1 × 4 antenna array.

antenna is 0.77 ~ 0.84 in the desired 5G mmWave band shown in Table 2.

B. ANTENNA ARRAY MEASUREMENT

The measured reflection coefficients ($|S_{11}|$ and $|S_{22}|$) and gain values of a 1 × 4 antenna array are shown in Fig. 17 and 18, respectively. The measured and simulated $|S_{11}|$ and $|S_{22}|$ values match very well. This shows that the design target of the international 5G mmWave frequency bands is covered. The measured H-/V-pol gain values were 10 ~ 11 dBi and the measured cross-pol suppression was

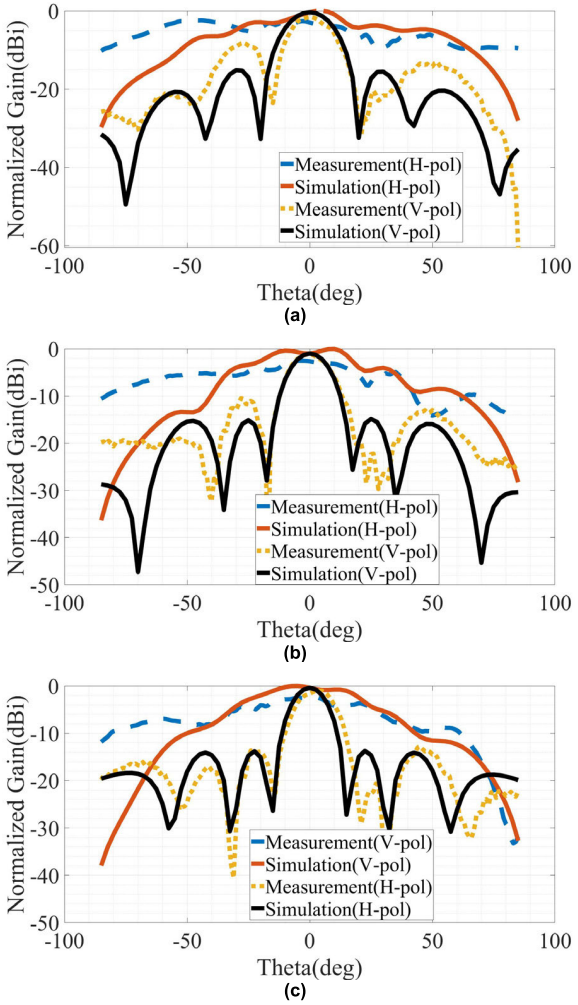

FIGURE 19. Measured radiation patterns of the proposed 1 ×4 antenna array at (a) 24 GHz, (b) 26 GHz, and (c) 28 GHz.

about 20 dB. Fig. 19 shows the normalized radiation patterns at 24, 26, and 28 GHz. The measured 3 dB beamwidth was

12° in azimuth (H-pol) and 60° in elevation (V-pol). All the design specifications in Table 2 were covered by the proposed antenna.

The performance of recently reported research on 5G mmWave antennas is summarized in Table 4 for comparison. The antenna designs reported in [11], [15] have relatively high antenna gain values. In [11], it needs a thick dielectric superstrate ($0.54\lambda_0$) to improve antenna gain which is much thicker than commercial mobile devices. In [15], its theoretical antenna gain value of the 1×4 array is about 13.7 dBi but its area (width $\times$ length) is almost two-times larger than the proposed antenna array. Most of the reported antenna designs have met the bandwidth and gain requirements of the 5G mmWave antenna module for mobile devices, but only a few of the reported antennas had dual polarization for the polarization diversity of MIMO. The proposed antenna satisfies all 5G mmWave requirements and is printed on FR4 substrate which is an extremely cost-effective material. It should be noted that the tan δ of FR4 substrate is about 30 times higher than that of the low-loss substrate materials.

V. CONCLUSION

The design and analysis of a broadband dual polarized patch antenna on FR4 substrate were presented in this study. Accurate electrical characterization of the FR4 substrate in the 5G mmWave frequency band was also presented. A proximity L-probe-fed structure and parasitic patches were designed to improve the -10 dB impedance bandwidth of a square patch antenna, and the measured fractional bandwidth of the proposed antenna was 23.1 % (23 $\sim$ 29 GHz). The effect of FR4 substrate's high tan δ was minimized by introducing an air cavity structure, and relatively high antenna gain was achieved (Single: 5 dBi, 1×4, Array: 11 dBi). Dual polarization capability for MIMO was implemented by exciting orthogonal resonant modes through symmetric antenna geometry. The operation principle of the proposed antenna was thoroughly investigated through CMA and the total surface current distributions. The proposed antenna satisfies all the design requirements of a 5G mmWave antenna module for mobile devices.

REFERENCES

[1] A. L. Swindlehurst, E. Ayanoglu, P. Heydari, and F. Capolino, "Millimeter-wave massive MIMO: The next wireless revolution?" *IEEE Commun. Mag.*, vol. 52, no. 9, pp. 56–62, Sep. 2014.

[2] T. E. Bogale and L. B. Le, "Massive MIMO and mmWave for 5G wireless HetNet: Potential benefits and challenges," *IEEE Veh. Technol. Mag.*, vol. 11, no. 1, pp. 64–75, Mar. 2016.

[3] F. Al-Ogaili and R. M. Shubair, "Millimeter-wave mobile communications for 5G: Challenges and opportunities," in *Proc. IEEE Int. Symp. Antennas Propag. (APSURSI)*, Fajardo, Puerto Rico, Jun. 2016, pp. 1491–1947.

[4] A. Ghosh, T. A. Thomas, M. C. Cudak, R. Ratasuk, P. Moorut, F. W. Vook, T. S. Rappaport, G. R. MacCartney, S. Sun, and S. Nie, "Millimeter-wave enhanced local area systems: A high-data-rate approach for future wireless networks," *IEEE J. Sel. Areas Commun.*, vol. 32, no. 6, pp. 1152–1163, Jun. 2014.

[5] S. Rangan, T. S. Rappaport, and E. Erkip, "Millimeter-wave cellular wireless networks: Potentials and challenges," *Proc. IEEE*, vol. 102, no. 3, pp. 366–385, Mar. 2014.

[6] E. Park and S. Kim, "Design and analysis of a TEM mode rectangular coaxial waveguide for mobile 5G millimeter wave antenna module applications," *J. Electromagn. Eng. Sci.*, vol. 20, no. 3, pp. 169–175, Jul. 2020.

[7] B. van Liempd, A. Visweswaran, S. Ariumi, S. Hitomi, P. Wambacq, and J. Craninckx, "Adaptive RF front-ends using electrical-balance duplexers and tuned SAW resonators," *IEEE Trans. Microw. Theory Techn.*, vol. 65, no. 11, pp. 4621–4628, Nov. 2017.

[8] J.-C. Chiu, S.-C. Hsiao, P.-K. Tseng, Y.-C. Lai, and C.-W. Huang, "An ultracompact, low-cost, and high-performance RF package technique for Wi-Fi FEM applications," *IEEE Microw. Wireless Compon. Lett.*, vol. 30, no. 3, pp. 265–267, Mar. 2020.

[9] G. Tian, J. Li, F. Hou, W. Zhang, X. Guo, L. Cao, and L. Wan, "Design and implementation of a compact 3-D stacked RF front-end module for micro base station," *IEEE Trans. Compon., Package. Manuf. Technol.*, vol. 8, no. 11, pp. 1967–1978, Nov. 2018.

[10] D. Liu, X. Gu, C. W. Baks, and A. Valdes-Garcia, "Antenna-in-package design considerations for Ka-band 5G communication applications," *IEEE Trans. Antennas Propag.*, vol. 65, no. 12, pp. 6372–6379, Dec. 2017.

[11] O. M. Haraz, A. Elboushi, S. A. Alshebeili, and A.-R. Sebak, "Dense dielectric patch array antenna with improved radiation characteristics using EBG ground structure and dielectric superstrate for future 5G cellular networks," *IEEE Access*, vol. 2, pp. 909–913, 2014.

[12] M. Asaadi and A. Sebak, "Gain and bandwidth enhancement of 2×2 square dense dielectric patch antenna array using a holey superstrate," *IEEE Antennas Wireless Propag. Lett.*, vol. 16, no. 3, pp. 1808–1811, Mar. 2017.

[13] J. Xu, W. Hong, Z. H. Jiang, H. Zhang, and K. Wu, "Low-profile wideband vertically folded slotted circular patch array for Ka-band applications," *IEEE Trans. Antennas Propag.*, vol. 68, no. 9, pp. 6844–6849, Sep. 2020.

[14] J. Xu, W. Hong, Z. H. Jiang, and H. Zhang, "Wideband, low-profile patch array antenna with corporate stacked microstrip and substrate integrated waveguide feeding structure," *IEEE Trans. Antennas Propag.*, vol. 67, no. 2, pp. 1368–1373, Feb. 2019.

[15] I. J. Hwang, H. W. Jo, B. K. Ahn, J. Oh, and J. Yu, "Cavity-backed stacked patch array antenna with dual polarization for mmWave 5G base stations," in *Proc. 13th Eur. Conf. Antennas Propag. (EuCAP)*, Krakow, Poland, Jun. 2019, pp. 1–5.

[16] R. G. Vaughan, "Polarization diversity in mobile communications," *IEEE Trans. Veh. Technol.*, vol. 39, no. 3, pp. 177–186, Aug. 1990.

[17] K.-P. Latti, M. Kettunen, J.-P. Strom, and P. Silventoinen, "A review of microstrip T-resonator method in determining the dielectric properties of printed circuit board materials," *IEEE Trans. Instrum. Meas.*, vol. 56, no. 5, pp. 1845–1850, Oct. 2007.

[18] I. Nadeem and D.-Y. Choi, "Study on mutual coupling reduction technique for MIMO antennas," *IEEE Access*, vol. 7, pp. 563–586, 2019.

[19] W.-S. Tung, P.-Z. Rao, and W.-M. Chen, "A millimeter-wave antenna on low cost FR4 substrate," in *Proc. IEEE Asia–Pacific Microw. Conf. (APMC)*, Singapore, Dec. 2019, pp. 652–653.

[20] W.-S. Tung, W.-Y. Chiang, C.-K. Liu, C.-A. Chen, P.-Z. Rao, P. A. R. Abu, W.-M. Chen, F. Asadi, and S.-L. Chen, "Low cost AIP design in 5G flexible antenna phase array system application," *Micromachines*, vol. 11, no. 9, p. 851, Sep. 2020.

[21] G. Kumar and K. Gupta, "Broad-band microstrip antennas using additional resonators gap-coupled to the radiating edges," *IEEE Trans. Antennas Propag.*, vol. 32, no. 12, pp. 1375–1379, Dec. 1984.

[22] J. Park, H.-G. Na, and S.-H. Baik, "Design of a modified L-probe fed microstrip patch antenna," *IEEE Antennas Wireless Propag. Lett.*, vol. 3, pp. 117–119, 2004.

[23] M. Vogel, G. Gampala, D. Ludick, U. Jakobus, and C. J. Reddy, "Characteristic mode analysis: Putting physics back into simulation," *IEEE Antennas Propag. Mag.*, vol. 57, no. 2, pp. 307–317, Apr. 2015.

[24] D.-W. Kim and S. Nam, "Systematic design of a multiport MIMO antenna with bilateral symmetry based on characteristic mode analysis," *IEEE Trans. Antennas Propag.*, vol. 66, no. 3, pp. 1076–1085, Mar. 2018.

[25] R. Garbacz and R. Turpin, "A generalized expansion for radiated and scattered fields," *IEEE Trans. Antennas Propag.*, vol. 19, no. 3, pp. 348–358, May 1971.

[26] R. Harrington and J. Mautz, "Theory of characteristic modes for conducting bodies," *IEEE Trans. Antennas Propag.*, vol. 19, no. 5, pp. 622–628, Sep. 1971.

[27] M. Khan and M. Chowdhury, "Analysis of modal excitation in wideband slot-loaded microstrip patch antenna using theory of characteristic modes," *IEEE Trans. Antennas Propag.*, vol. 68, no. 11, pp. 7618–7623, Nov. 2020.

[28] E. Safin and D. Manteuffel, "Manipulation of characteristic wave modes by impedance loading," *IEEE Trans. Antennas Propag.*, vol. 63, no. 4, pp. 1756–1764, Apr. 2015.
[29] Y. Cao, Y. Cai, W. Cao, B. Xi, Z. Qian, T. Wu, and L. Zhu, "Broadband and high-gain microstrip patch antenna loaded with parasitic mushroom-type structure," *IEEE Antennas Wireless Propag. Lett.*, vol. 18, no. 7, pp. 1405–1409, Jul. 2019.
[30] T. A. Milligan, *Modern Antenna Design*, 2nd ed. Hoboken, NJ, USA: Wiley, Jul. 2005.

GYOUNGDEUK KIM received the B.S. degree in electronics engineering from Pusan National University, South Korea, in 2020, where he is currently pursuing the M.S. degree. His current research interests include antenna design and RF systems.

SANGKIL KIM (Senior Member, IEEE) received the B.S. degree *(magna cum laude)* from the School of Electrical and Electronics Engineering, Yonsei University, Seoul, South Korea, in 2010, and the M.S. and Ph.D. degrees from the School of Electrical and Computer Engineering, Georgia Institute of Technology, GA, Atlanta, USA, in 2012 and 2014, respectively. From 2015 to 2018, he worked with Qualcomm, Inc., San Diego, CA, USA, as a Senior Engineer. He joined as a Faculty Member with the Department of Electronics Engineering, Pusan National University, Busan, South Korea, in 2018. He has published 32 articles in peer-reviewed journals and five book chapters. His main research interests include mmWave phased antenna array, machine learning assisted backscattering communication, RF biosensors, energy harvesting, and printed RF electronics. He is a member of the IEEE MTT-26 RFID, Wireless Sensors, and IoT Committee. He received the IET Premium Award Microwave, Antennas and Propagation, in 2015, and the KIEES Young Researcher Award, in 2019.